communications materials

Article

https://doi.org/10.1038/s43246-024-00660-8

Reducing inhomogeneous broadening of spin and optical transitions of nitrogen-vacancy centers in high-pressure, high-temperature diamond

Rémi Blinder[1], Yuliya Mindarava[1], Thai Hien Tran[2,10], Ali Momenzadeh[2,11], Sen Yang[2,12], Petr Siyushev[2,13], Hitoshi Sumiya[3], Kenji Tamasaku[4], Taito Osaka[4], Norio Morishita[5], Haruki Takizawa[5], Shinobu Onoda[5], Hideyuki Hara[6], Fedor Jelezko[1,7], Jörg Wrachtrup[2,8] & Junichi Isoya[9]

With their optical addressability of individual spins and long coherence time, nitrogen-vacancy (NV) centers in diamond are often called “atom-like solid spin-defects”. As observed with trapped atomic ions, quantum interference mediated by indistinguishable photons was demonstrated between remote NV centers. In high sensitivity DC magnetometry at room temperature, NV ensembles are potentially rivaling with alkali-atom vapor cells. However, local strain induces center-to-center variation of both optical and spin transitions of NV centers. Therefore, advanced engineering of diamond growth toward crystalline perfection is demanded. Here, we report on the synthesis of high-quality HPHT (high-pressure, high-temperature) crystals, demonstrating a small inhomogeneous broadening of the spin transitions, of $T_2^* = 1.28$ μs, approaching the limit for crystals with natural ^{13}C abundance, that we determine as $T_2^* = 1.48$ μs. The contribution from strain and local charges to the inhomogeneous broadening is lowered to ~17 kHz full width at half maximum for NV ensemble within a > 10 mm^3 volume. Looking at optical transitions in low nitrogen crystals, we examine the variation of zero-phonon-line optical transition frequencies at low temperatures, showing a strain contribution below 2 GHz for a large fraction of single NV centers.

The electron spin of the negatively charged nitrogen-vacancy (NV) center is one of the leading platforms for quantum technology applications due to outstanding properties allowing optical initialization and readout, coherent manipulation by microwave pulses, and a long coherence time. As a material, diamond is an ideal host for electron spin qubits, because of its high Debye-temperature (due to strong covalent bonding), its weak spin-orbit coupling for the carbon orbitals, and the low natural abundance of magnetic nuclei (^{13}C: 1.07%). All these factors make environmental fluctuations small and their coupling to the electron spin weak. However, the optical and spin properties of NV centers can be affected by imperfections of the host crystal such as the presence of other paramagnetic spin species, and crystalline quality (strain). Since “quantum-grade” purity with the concentration of substitutional nitrogen (N_s^0, $S = 1/2$) < 1 ppb is attainable, homoepitaxial diamond films grown by microwave plasma assisted chemical vapor deposition (MPCVD) are the primary source of material for quantum applications[1–3]. With this technique, besides the high purity,

---

[1]Institute for Quantum Optics, Ulm University, 89081 Ulm, Germany. [2]3rd Institute of Physics, University of Stuttgart, 70569 Stuttgart, Germany. [3]Sumitomo Electric Industries Ltd., Itami, Hyogo, 664-0016, Japan. [4]RIKEN SPring-8 Center, 1-1-1 Kouto, Sayo-cho, Sayo-gun, Hyogo, 679-5148, Japan. [5]Quantum Materials and Applications Research Center, National Institutes for Quantum Science and Technology, Takasaki, Gunma, 370-1292, Japan. [6]Bruker Japan K.K., Yokohama, Kanagawa, 221-0022, Japan. [7]Centre for Integrated Quantum Science and Technology (IQST), 89081 Ulm, Germany. [8]Max Planck Institute for Solid State Research, 70569 Stuttgart, Germany. [9]Faculty of Pure and Applied Sciences, University of Tsukuba, Tsukuba, Ibaraki, 305-8573, Japan. [10]Present address: Quantum Machines Germany, Liebknechtstraße 33, 70565 Stuttgart, Germany. [11]Present address: Robert Bosch GmbH, 72770 Reutlingen, Germany. [12]Present address: Department of Physics, The Hong Kong University of Science and Technology, Clear Water Bay, Kowloon, Hong Kong, China. [13]Present address: Institute for Materials Research (IMO), Hasselt University, 3590 Diepenbeek, Belgium. e-mail: remi.blinder@uni-ulm.de

^{12}C-enrichment[1–3], preferential orientation[4], as-grown flat surface[3], and delta-doping[5,6] were achieved. However, the presence of crystal defects (strain) is still an impediment in the context of some quantum applications.

Growth of large (~6 mm) colorless synthetic diamonds by the temperature gradient method in high-pressure and high-temperature (HPHT) growth was reported in 1972[7]. Large type-IIa crystals (~7 mm) with the content in impurities (N, B, Ni) < 0.1 ppm were realized in 1996[8]. Recently, larger (~12 mm), high-crystalline-quality crystals with low density of dislocations and stacking faults were grown[9]. Large, type-IIa HPHT crystals of high crystalline quality are demanded for designing the optical elements of synchrotron X-ray radiation beam applications[10]. The present work demonstrates that HPHT diamonds of such quality could make up for the currently immature part of the CVD (chemical vapor deposition) growth technology with respect to lowering the density of dislocation toward crystalline perfection.

In DC magnetometry using NV ensembles, the inhomogeneous broadening ($1/T_2{}^*$ in time domain) of the optically detected magnetic resonance (ODMR) spectrum limits the sensitivity. By using CVD diamonds with low nitrogen concentrations, it was inferred that ^{13}C spins at natural abundance limit the dephasing time so that $T_2{}^* \le 1$ μs[11], however, the ^{13}C-determined limit has not been precisely established. In the present investigation, by using high-crystalline-quality HPHT diamond decreasing unwanted contributions to the dephasing time such as strain, $T_2{}^* = 1.28$ μs is obtained. Besides, $T_2{}^* = 1.48$ μs is found as the ^{13}C-determined limit for natural abundance.

Long-distance entanglement protocol for quantum networks, which could use NV centers, rely crucially on the spin-photon interface[12] and indistinguishable photons from remote spins[13,14]. At low temperatures (< 10 K), the zero-phonon line (ZPL) of NV consists of distinct six resonant lines split by spin-orbit coupling, spin-spin interaction, and transverse strain ($\delta_\perp$)[15]. A low strain environment ($\delta_\perp \lesssim 2$ GHz) provides high-fidelity initialization and readout[12,16]. Although dc Stark-shift tuning is applicable[17,18], narrowing down the distribution of the ZPL frequencies caused by strain is desired. In the present work, single NV centers were created by low fluence electron irradiation and subsequent annealing in high-crystalline-quality and high-purity HPHT crystals of $[\mathrm{N_s}^0]$=3 ~ 4 ppb. A large fraction of single NV centers show $\delta_\perp$<2 GHz.

Results

Inhomogeneous broadening of NV spin transitions in a high-quality HPHT crystal

The inhomogeneous broadening of the electron spins resonant transitions constitutes one of the factors that limits the sensitivity of DC magnetometry based on NV ensembles (among others, such as the NV center density and optical readout contrast)[11]. The resonance frequencies of single NV centers can be determined from the spin Hamiltonian, which reads (neglecting ^{14}N hyperfine and nuclear Zeeman interactions)

$$\begin{aligned}\hat{H} = {} & \mu_B \mathbf{B}^{\mathrm{T}} g \hat{\mathbf{S}} + D\hat{S}_z^2 + \varepsilon_z \hat{S}_z^2 + \varepsilon_x\left(\hat{S}_y^2 - \hat{S}_x^2\right) + \varepsilon_y\left(\hat{S}_x\hat{S}_y + \hat{S}_y\hat{S}_x\right) \\ & + \varepsilon'_x\left(\hat{S}_x\hat{S}_z + \hat{S}_z\hat{S}_x\right) + \varepsilon'_y\left(\hat{S}_y\hat{S}_z + \hat{S}_z\hat{S}_y\right) + \hat{H}_{\mathrm{NV-bath}},\end{aligned} \qquad (1)$$

where $\mathbf{B}$ is the external magnetic field, g is the g-tensor, $g_{||} = 2.0029$, $g_\perp = 2.0031$[19] where the "||" subscript indicates the [111] crystal direction (z axis), D is the zero-field splitting of the NV center, the terms ε_x, ε_y, ε_z, ε'_x, ε'_y are related to strain or electric field. In case of an electric field $\mathbf{\Pi} = (\Pi_x, \Pi_y, \Pi_z)$, one has $(\varepsilon_x, \varepsilon_y, \varepsilon_z) = (d_\perp \Pi_x, d_\perp \Pi_y, d_{||}\Pi_z)$ with $d_{||} = 0.35$ Hz·cm·V^{-1} and $d_\perp = 17$ Hz·cm·V^{-1} [20,21], and $(\varepsilon'_x, \varepsilon'_y) = (d'_\perp \Pi_x, d'_\perp \Pi_y)$. To our knowledge, $d'_\perp$ has not been experimentally determined, however, it is expected to be of the same order of magnitude as $d_\perp$[22,23]. $\hat{H}_{\mathrm{NV-bath}}$ describes the magnetic coupling between NV and the "bath" of paramagnetic species, that includes ^{13}C nuclei ($I = 1/2$, natural abundance 1.07%), electron spins such as isolated substitutional nitrogen $\mathrm{N_s}^0$ (also called P1 centers), neighboring NV centers.

Different NV centers will not have their Hamiltonian parameters exactly equal in magnitude, leading to a spread in the transition frequencies. In the case of Lorentzian broadening, the decay of the FID (free induction decay) is single exponential with $T_2{}^* = 1/[\pi \Delta\nu_{1/2}]$ where $\Delta\nu_{1/2}$ is the full-width at half-maximum (FWHM). The dephasing time $T_2{}^*$ of ensemble NV is determined by several contributions[11],

$$\begin{aligned}\frac{1}{T_2^*} \approx {} & \left[\frac{1}{T_2^*}\right]_{^{13}\mathrm{C}} + \left[\frac{1}{T_2^*}\right]_{\mathrm{N_s^0}} + \left[\frac{1}{T_2^*}\right]_{\mathrm{X}} + \left[\frac{1}{T_2^*}\right]_{\mathrm{NV-NV}} \\ & + \left[\frac{1}{T_2^*}\right]_{\mathrm{strain}} + \left[\frac{1}{T_2^*}\right]_{\mathrm{charges}} + \left[\frac{1}{T_2^*}\right]_{B-\mathrm{inhom}} + \frac{1}{T_2}.\end{aligned} \qquad (2)$$

The first four terms represent the contribution of the coupling to the spin bath, that is NV-^{13}C, NV-$\mathrm{N_s}^0$, NV-NV or NV-X interaction, using 'X' to denote paramagnetic spins other than $\mathrm{N_s}^0$ or NV. The fifth and sixth terms represent the contributions from lattice strain and the coupling to electric fields generated by local charges[21,22,24]. The seventh and eighth terms describe the contributions from the magnetic field inhomogeneity over the sample volume and decoherence.

Bath spins, in general, induce a local magnetic field on the NV center. This magnetic field varies from one center to another due to changing spatial arrangement of the bath species, and variation in their quantum state (e.g. $m_{\mathrm{I}} = -½$ of $+½$ for a ^{13}C nuclear spin, $I = 1/2$), ultimately leading to inhomogeneous broadening. In the case of dilute bath spins (of fraction $x < 0.01$), each contribution gives a Lorentzian broadening proportional to the spin concentration[11,25]. For instance, considering the two first contributions, one can write:

$$\left[\frac{1}{T_2^*}\right]_{13\mathrm{C}} = A_{13\mathrm{C}}\left[{}^{13}\mathrm{C}\right], \qquad (3)$$

$$\left[\frac{1}{T_2^*}\right]_{\mathrm{N_s^0}} = A_{\mathrm{N_s^0}}\left[\mathrm{N_s^0}\right]. \qquad (4)$$

A reliable value of $A_{\mathrm{N_s^0}}$ was experimentally obtained as 101 ± 12 ms^{-1}ppm^{-1}, since $T_2{}^*$ was measured for a wide range of $[\mathrm{N_s}^0]$ in samples in which $T_2{}^*$ is predominantly determined by $\mathrm{N_s}^0$[11,26]. On the other hand, $A_{^{13}\mathrm{C}}$ has not been precisely determined, since preparing samples of a wide range of [^{13}C] with relatively small contributions of other sources is not easy.

Based on $T^*_{2,\mathrm{DQ}}$ (0.445 μs) measured for ensemble NV by double-quantum (DQ) Ramsey FID and considering $[\mathrm{N_s}^0]$=0.4 ppm, $A_{^{13}\mathrm{C}} \approx 0.100$ ms^{-1}ppm^{-1} was estimated[11,26]. In this measurement, the transverse and longitudinal strain contributions were suppressed by using a bias field of 150 G and DQ protocol, respectively. By using $A_{^{13}\mathrm{C}} \approx 0.100$ ms^{-1}ppm^{-1}, $T_2{}^*$ limited by natural abundance (^{13}C: 1.07%) evaluates to about ≈0.93 μs, so that the estimate "$T_2{}^* \approx 1$ μs (to better than 10%)" was retained[11].

However, a precise description of the FID in the regime where the hyperfine interaction from NV to surrounding ^{13}C largely dominates is still missing, in such samples with natural isotopic abundance. In the present work, the properties of ensemble NVs in a high-quality HPHT crystal (sample-A), with 1.07% ^{13}C, were investigated. We will outline several steps taken during the preparation of sample-A to mitigate the influence of all terms listed in Eq. (2), except for the ^{13}C contribution.

First, a method for creating NV (by conversion of $\mathrm{N_s}^0$ incorporated in diamond during growth) was chosen so as to induce minimal deterioration of the host crystal. A protocol, consisting of high temperature (800 °C) electron irradiation and subsequent annealing at 1000 °C (2 h in vacuum), was employed to lower the formation of residual paramagnetic radiation damages such as divacancy ($S = 1$) and vacancy chains ($S = 1$)[27]. This should help mitigating the third contribution in Eq. (2).

To mitigate the fifth contribution (strain) in Eq. (2), a high-quality HPHT sample of low density of crystal defects such as dislocations and

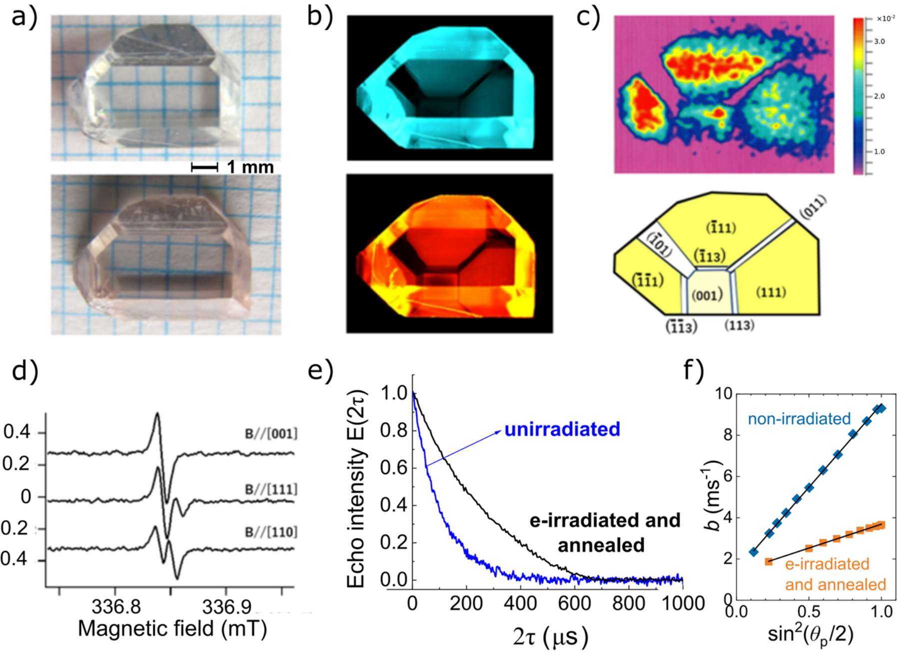

Fig. 1 | Characterization of sample-A. **a** Photographs of sample-A before and after NV formation. **b** Fluorescence image under short-wavelength UV (taken using DiamondView) before and after NV formation.**c** Top: EPR imaging of N_s^0 (before NV formation) exhibiting the growth sector dependence of the uptake of N_s^0. Bottom: Distribution of growth sectors. **d** Slow-passage, cw-EPR of the central line of ^{14}N hyperfine structure of N_s^0 demonstrating a narrow linewidth ($\Delta B_{pp} = 0.08$ G) enabling to resolve the anisotropy of the central line position. With the C_{3v} symmetry, N_s^0 has magnetically distinguishable four symmetry-related sites. With **B**//[001] all four sites are equivalent. With **B**//[111] and **B**//[011], the central line splits into two lines with the intensity ratio 3:1 and 2:2, respectively, owing to the second-order effect of the ^{14}N hyperfine interaction and the g-anisotropy[28,29]. **e** Hahn-echo decay of N_s^0 before and after NV formation. **f** Instantaneous diffusion of N_s^0 before and after NV formation. The inverse of the time constant of two-pulse echo decay is plotted against $\sin^2(\theta_p/2)$ where θ_p is the flipping angle of the second MW pulse.

stacking faults was employed as base material. X-ray-topography measurements (Supplementary Information, section S4), indicate that sample-A has a low density of dislocations, ~200 cm^{-2}. Besides, the low strain character of sample-A is proved by the narrow EPR linewidth of N_s^0 measured before electron irradiation. The central line of the ^{14}N ($I = 1$) hyperfine structure of N_s^0 in slow-passage, X-band, continuous wave (CW) EPR spectrum of unirradiated sample-A is shown in Fig. 1d. A narrow linewidth ($\Delta B_{pp} = 0.08$ G) reveals the anisotropy of the central line position (resulting from the second order effect of the ^{14}N hyperfine interaction, and a weak g-anisotropy[28,29]) which was reported so far by using ^{12}C-enriched crystals[28].

To reduce the impact of the second contribution in Eq. (2), we used a crystal with low N_s^0 density. The uptake of nitrogen in sample-A and the resulting formation region for NV centers are confined in the {111} and {100} growth sectors as revealed by the fluorescence image under short-wavelength UV excitation shown in Fig. 1b, taken using DiamondView (Diamond Trading Company, De Beers Ltd.)[30]. EPR imaging shown in Fig. 1c indicates that the local N_s^0 concentration, $[N_s^0]_{loc}$ is similar between the {111} and {100} sectors. Both before irradiation, and after irradiation followed by annealing, $[N_s^0]_{loc}$ was obtained by utilizing the instantaneous spectral diffusion effect in two-pulse echo decay[31,32], which is an effective method for extracting the local concentration using pulsed EPR. Being free of power-saturation effects, pulsed EPR yields, for paramagnetic species of long spin-lattice relaxation time, more precise spin number determination than CW-EPR techniques. The instantaneous diffusion method also circumvents the need for a reference sample. Two-pulse echo decay measured as a function of the flipping angle (θ_p) of the second microwave (MW) pulse consists of flipping-angle-dependent and independent terms:

$$E(2\tau) \propto \exp(-2b\tau)\exp\left(-(2\kappa\tau)^{\beta}\right), \qquad (5)$$

where the second term represents spectral diffusion induced by random spin flips of neighboring spins, while the decay rate in the first term is related to the instantaneous spectral diffusion effect[31,32]:

$$b = \frac{\pi}{9\sqrt{3}} \frac{\mu_0 (g\mu_B)^2}{\hbar} C \sin^2\left(\theta_p/2\right) + b_0, \qquad (6)$$

where C is the volume concentration of the $S = 1/2$ electron spins excited by the MW pulses and b_0 is a parameter that represents an additional background exponential contribution. The datasets acquired at different θ_p are fitted globally to the model in Eq. (5), where b is allowed to vary across datasets, see Supplementary Information (SI), Section S5.1. The concentration C is then extracted by a linear fit of b as shown in Fig. 1f. Considering that only one of the ^{14}N hyperfine lines is excited by the MW pulses, it is obtained that $[N_s^0]_{loc}$ is 166 ± 2 ppb and 47 ± 2 ppb before irradiation and after irradiation followed by annealing, respectively (Fig. 1e, f). After irradiation and annealing, acquisition with pulsed EPR of transient echoes of NV and N_s^0 in the dark allows estimating the overall number of spins ratio of NV over N_s^0, which is found equal to 0.41 (see SI, section S5.2). Since NV centers are created in the growth sectors where nitrogen is present, that is {111} and {100} (Fig. 1c), it follows that $[NV]_{loc} = 0.41 \times 47 = 19 \pm 1$ ppb (using the above determination of $[N_s^0]_{loc}$).

Last, while we also expect the neutral charge state NV^0 ($S = 1/2$) to be formed, the contribution of NV^0 centers to the decay rate ($1/T_2^*$) of negatively charged NV centers (via the third term in Eq. (2)) is likely to be negligibly small, indeed, the dipolar field from NV^0 is averaged out due to its short spin-lattice relaxation time caused by the dynamic Jahn–Teller effect[33].

The present study of the T_2^* of NV centers is based on pulsed EPR measurements at X-band (~9.7–9.8 GHz). EPR allows manipulation of spins with fairly homogeneous driving and static bias fields within large sample volumes (several tens of mm^3), and thus enables high-throughput, high S/N ratio, investigation of macroscopic samples. With pulsed EPR, one can record T_2^* decays as time domain transients (FID or spin echo), that are equivalent to a Ramsey measurement[11]. Figure 2a compares the FID with the outcome of the Hahn echo sequence for sample-A—where the echo signal is recorded from its maximum, therefore representing half of the full echo. The crystal was aligned to bring the magnetic field close (<1°) to the NV axis ([111]) for one out of the four possible NV orientations. The magnetic field value ($B = 2436$ G) was set so that the MW frequency ($\nu_{MW} = 9.7$ GHz) matches, for the $m_S = 0 \leftrightarrow +1$ transition of this NV center subset, the central line of the ^{14}N ($I = 1$) hyperfine structure. We used constant 200 mW laser illumination (532 nm) to enhance the NV signal ~800 times, enabling faster data acquisition. All three ^{14}N hyperfine lines were excited owing to the large Rabi frequency ($\Omega_1 = (2\pi)$ 25 MHz). The initial part (~100 ns) of

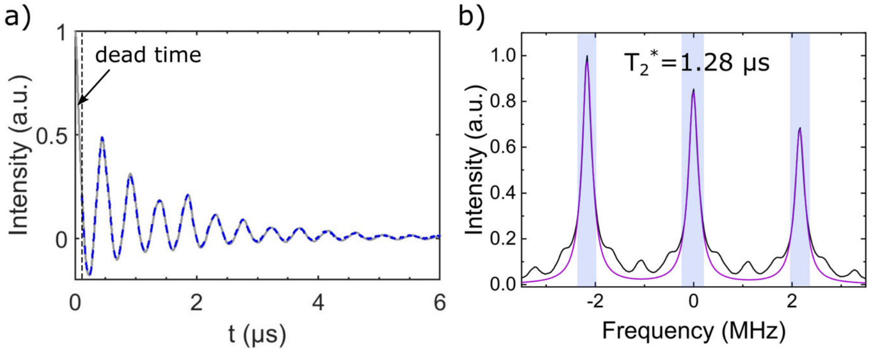

Fig. 2 | Half-echo and FFT of ensemble NV in sample-A. a Superposition of half-echo (gray solid) measured with Hahn echo sequence and FID (blue dashed) for ensemble NV in low-strain HPHT crystal (sample-A) with **B**//[111]. In both cases, the signal corresponds to the real part, that is the dominant quadrature after phasing. The initial points (first ~100 ns) of the FID, within the EPR spectrometer's deadtime, are not recorded. **b** Spectrum obtained by FFT of half-echo (black) and fit of NV primary lines with three Lorentzian functions with equal linewidth (purple). The spectrum corresponds to the real part of the FFT, computed from both quadratures of the echo signal. The blue shaded areas with a width of 360 kHz each correspond to the fitted regions of the spectrum. The value of T_2^* estimated from the fit is 1.280 ± 0.016 μs.

the FID is not detected, which corresponds to the so-called deadtime, typical of EPR experiments.

To obtain the spectrum, Fast Fourier Transform (FFT) was implemented using half-echo, as using the FID would result in spectral distortion due to the information lost during the deadtime. The FFT spectrum consists of three primary lines, as expected, corresponding to the three possible states of the ^{14}N nuclear spin ($m_I = -1, 0, +1$), with a separation very well matching the known hyperfine (hf) splitting, $|A_{hfs}| = 2.14$ MHz[19]. The primary lines themselves are well described by a set of Lorentzian functions of equal width, as illustrated by the fit in Fig. 2b. Uneven intensities among these lines is a typical feature of EPR spectra acquired under optical pumping of the NV center and reflects nuclear spin polarization of the ^{14}N[34]. The fit yields $\Delta\nu_{1/2}$ of 248.7 ± 3.1 kHz as the Lorentzian width (FWHM), which corresponds to T_2^* of 1.280 ± 0.016 μs ($T_2^* = 1/[\pi\Delta\nu_{1/2}]$).

We now discuss quantitatively the possible contributions to the observed broadening of the primary lines from the various terms in Eq. (2). First, we consider the inhomogeneity of the externally applied magnetic field over the NV ensemble volume, corresponding to the term $\left[\frac{1}{T_2^*}\right]_{B-\text{inhom}}$. This inhomogeneity, ΔB, provides a contribution to the broadening $\Delta\nu_{1/2,B\text{-inhom}} = g_{||}\mu_B\Delta B$. Within sample-A, as described in the Methods section, we determined $\Delta B/B = 1.83 \pm 0.73$ ppm. For the magnetic field applied in the present acquisition ($B = 2436$ G), it corresponds to $\Delta\nu_{1/2,B\text{-inhom}} = 12.5 \pm 4.9$ kHz. As we see as well from Eq. (2), the interaction of NV to different electron spin species (N_s^0, "X", or other NVs) can participate in the T_2^* process. Using the value $A_{Ns0} = 101$ ms^{-1}·ppm-1 (ref. 11, 26), the interaction with neutral substitutional nitrogen ($[N_s^0]_{loc} = 0.047$ ppm) is expected to yield $T_2^* = 210$ μs ($\Delta\nu_{1/2} = 1.51$ kHz). Similarly, one can consider the fourth term in Eq. (2), that represents the effect of NV-NV interaction. Based on considerations of the spin multiplicity, and on the possibility of having both resonant and off-resonant NVs, 165 ms^{-1}ppm^{-1} < A_{NV} < 245 ms^{-1}ppm^{-1} was estimated[11]. With the obtained value $[NV]_{loc} = 0.019$ ppm, the T_2^* determined by NV-NV interaction therefore evaluates to 214 μs < T_2^* < 319 μs, corresponding to 0.99 kHz < $\Delta\nu_{1/2,\text{ NV-NV}}$ < 1.48 kHz. In addition, as remarked earlier, the high temperature irradiation technique should lead to very low density of defects such as divacancies ($S = 1$) or vacancy clusters ($S = 1$), thus we expect the third term in Eq. (2) to be negligible. Following measurement of the Hahn echo decay of NV, we determine that the broadening contribution from the last term ($1/T_2$) in Eq. (2), verifies $\Delta\nu_{1/2,T_2} = 1/[\pi T_2]$ < 0.75 kHz (see SI, section S5.3).

We now turn our attention to the contribution from strain and local charges. To separate this contribution from that of the other terms in Eq. (2), a possibility is to use the DQ protocol. This protocol relies on observing the dephasing in the DQ basis {+1, −1}, which typically is performed by applying MW pulses of two different frequencies, corresponding to the $|0\rangle \leftrightarrow |+1\rangle$ and $|0\rangle \leftrightarrow |-1\rangle$ transitions respectively, in order to create the coherent state superposition $(1/\sqrt{2})(|-1\rangle+|+1\rangle)$[11,26]. The broadening due to the longitudinal strain or electric field (term ε_z), which causes common energy shift in both $m_S = -1$ and $m_S = +1$ states, is suppressed. Moreover, setting a magnetic field along the NV axis, so that $g_{||}\mu_B B \gg |\varepsilon_x|, |\varepsilon_y|$ and avoiding the magnetic field of the ground state level anticrossing or GSLAC (at $B_{gs} = D/g_{||}\mu_B \sim 1024$ G) ensures that the transverse terms $\varepsilon_x, \varepsilon_y, \varepsilon'_x, \varepsilon'_y$ are removed (SI, section S7). At the same time, the broadening due to the magnetic terms is enhanced by a factor of two, due to the $\Delta S_z = 2$ character of the transition[11,26]. For NV at $B > B_{gs}$, the transition frequencies obey $\nu_{10} - \nu_{-10} = 2D = 5.74$ GHz (SI, section S7), which poses a challenge for applying the DQ protocol with single frequency systems, such as in conventional EPR. Here, as a workaround, we use the possibility to excite the "forbidden" $\Delta S_Z \approx 2$ transition, where "forbidden" refers to the weaker transition dipole (in comparison to usual or "allowed" transitions), and Z is the axis of the magnetic field, possibly tilted from the NV axis, z. This transition appears in the spectral region labeled in the EPR literature as "half-field" (due to its resonant magnetic field, $B \sim h\nu_{MW}/2\, g\mu_B$, being roughly half of that of the bare electron $g = 2.0024$ resonance)[35], however, with the magnetic field aligned to the NV axis, the transition probability is zero. The ingredient required for having a non-zero probability is a weak degree of mixing in the spin eigenstates, which can be obtained by tilting the magnetic field slightly away from the NV axis. Indeed, with a small tilt (Θ), $|-1\rangle$, $|+1\rangle$ evolve into different eigenstates reading, at first order in Θ, $|-1_\Theta\rangle = |-1\rangle + \eta_{-10}|0\rangle$, $|+1_\Theta\rangle = |+1\rangle + \eta_{10}|0\rangle$ (see SI, section S8.1). This implies that the $|-1_\Theta\rangle \leftrightarrow |+1_\Theta\rangle$ transition can be driven by MW pulses of single frequency. Thus, we now describe how is extracted the inhomogeneous broadening of the half-field transition, $\Delta\nu_{1/2,\text{half-field}}(\Theta)$. In the limit Θ~0, it is expected to converge towards that in the {+1, −1} basis, that we label $\Delta\nu_{1/2,DQ}$.

Figure 3 shows echoes and the corresponding FFT spectra obtained on the forbidden $\Delta S_Z \approx 2$ transition for different magnetic field tilts down to Θ=3° (full echoes are recorded instead of half-echo as in Fig. 2, which helps in improving S/N for the weak, forbidden transitions). The magnetic field and microwave frequency were adjusted to excite the central line of the ^{14}N hyperfine structure ($m_I = 0$). Owing to the low transition dipole of the forbidden transition, the attainable Rabi frequency at a certain microwave power is reduced compared to the allowed case. Here, at each value of Θ, the MW power was adjusted to ensure a constant Rabi drive, $\Omega_1 = (2\pi)$ 3.125 MHz. The central primary line ($m_I = 0$ for ^{14}N) lies well within the excitation bandwidth, which is important to avoid distortion in the echo/FFT for this contribution. Lorentzian fits of the central line provides the dependency $\Delta\nu_{1/2,\text{half-field}}(\Theta)$, as shown in Fig. 3b. We note that the outer ^{14}N lines, $m_I = -1, +1$, are far detuned and thus imperfectly driven. Considering that $\Delta\nu_{1/2,\text{half-field}}$ should be an even function with respect to Θ, we perform a quadratic fit, $\Delta\nu_{1/2,\text{half-field}}(\Theta) = \Delta\nu_{1/2,DQ} + c\Theta^2$. The latter yields $\Delta\nu_{1/2,DQ} = 456.6 \pm 10.0$ kHz corresponding to $T^*_{2,DQ} = 0.697 \pm 0.014$ μs ($1/[\pi\Delta\nu_{1/2,DQ}]$). The data shows a downward evolution trend of $\Delta\nu_{1/2,\text{half-field}}$ with Θ ($c < 0$), which we attribute to the increase in the degree of state

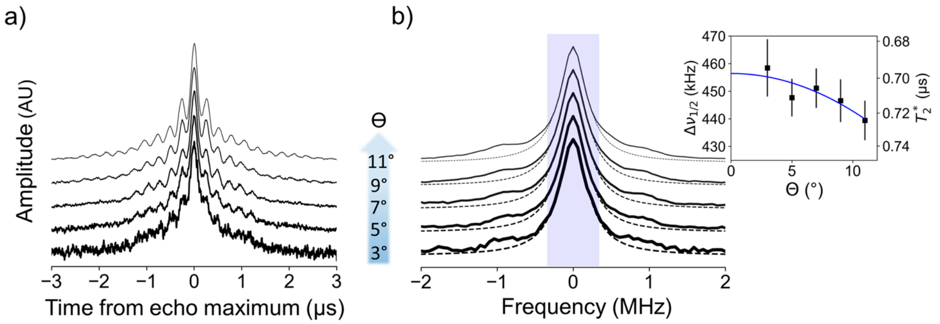

Fig. 3 | Echoes and FFT for the forbidden ($\Delta S_Z \approx 2$) transition of ensemble NV in sample-A, at different tilt angles. **a** Echoes as a function of the tilt (Θ) of the magnetic field axis from the [111] direction. For clarity, traces are vertically offset and only the real quadrature is shown. **b** Left: spectrum obtained by FFT of echoes, where both real and imaginary parts were used to compute the spectrum and only the real part of the FFT is shown. The frequency range, of 4 MHz width, is chosen to show the primary line corresponding to the $m_I = 0$ state of ^{14}N, and shoulders related to weakly coupled ^{13}C with $|A_{\mathrm{hfs}}| \sim 1$ MHz (the splitting equals $2|A_{\mathrm{hfs}}|$ due to the $\Delta S_Z \approx 2$ character of the transition). Due to the lower transition dipole for the forbidden transition compared to the allowed ones, the lines corresponding to $m_I = -1, +1$ (detuned by twice the amount compared to allowed transitions, $\sim \pm 2A_{^{14}\mathrm{N},||} = \pm 4.28$ MHz), as well as other ^{13}C satellites lines, are not efficiently driven. The dashed lines show Lorentzian fits of the primary line for each dataset, considering as fitting region the blue shaded area (of 720 kHz width) to extract $\Delta\nu_{1/2}(\Theta)$. Right: Lorentzian widths $\Delta\nu_{1/2}(\Theta)$ (with ±σ error bars), and quadratic fit using the function $\Delta\nu_{1/2}(\Theta) = \Delta\nu_{1/2,\mathrm{DQ}} + c\Theta^2$, allowing determination of the broadening ($\Delta\nu_{1/2,\mathrm{DQ}}$) in the basis $\{-1, +1\}$, as usually measured using the DQ protocol.

Table 1 | Separation of individual broadening contributions for ensemble NV in sample-A ($m_s = 0 \leftrightarrow +1$ transition at $B = 2436$ G)

	^{13}C	NV-N_s^0	NV-NV	strain	charges	B-inhom.	decoherence T_2
$\Delta\nu_{1/2}$ (kHz)	216(6)	1.51(4)	<1.48	15(6)	2.15(8)	12(5)	<0.75
T_2^* (μs)	1.48(4)	211(5)	>214	15 to 35	148(5)	18 to 42	>426

The listed broadening contributions correspond to the different sources in Eq. (2). Summation over the $\Delta\nu_{1/2}$ from each source matches the Lorentzian width of the primary line observed in Fig. 2 ($\Delta\nu_{1/2} = 248.7 \pm 3.1$ kHz). The second row reports, for each contribution, $T_2^* = 1/[\pi\ \Delta\nu_{1/2}]$.

mixing with the tilt (SI, section S8.1), lowering the impact of the magnetic interaction terms (such as the hyperfine interaction to ^{13}C) on the dephasing, and therefore resulting in lower inhomogeneous broadening upon increasing the tilt ($0 < \Theta < 11°$).

We calculate $T^*_{2,\mathrm{DQ}}/T^*_{2,\mathrm{allowed}} = \Delta\nu_{1/2,\mathrm{allowed}} / \Delta\nu_{1/2,\mathrm{DQ}} = 0.544 \pm 0.017$. This value is larger than the ratio (1/2) expected if the dephasing is caused solely by magnetic interactions such as NV-^{13}C, NV-N_s^0, NV-NV dipolar interactions and the external field inhomogeneity. The extra part of the dephasing in $\Delta\nu_{1/2,\mathrm{allowed}} = 248.7 \pm 3.1$ kHz occurs through the contribution of the terms due to strain and local charges in Eq. (2). In fact, the contribution from strain and charges can be estimated from the difference between $\Delta\nu_{1/2,\mathrm{allowed}}$ and $0.5 \times \Delta\nu_{1/2,\mathrm{DQ}}$. That is, $\Delta\nu_{1/2,\mathrm{strain+charges}} = \Delta\nu_{1/2,\mathrm{allowed}} - 0.5 \times \Delta\nu_{1/2,\mathrm{DQ}} - \delta_{\mathrm{inhom}}$, where $\delta_{\mathrm{inhom}} = 3.6 \pm 1.4$ kHz is a correction term accounting for the slightly lower inhomogeneity of the bias magnetic field in the DQ measurement (see Methods section). Subsequently, we obtain $\Delta\nu_{1/2,\mathrm{strain+charges}} = 17 \pm 6$ kHz. Local charges correspond to defects, such as neighboring NV centers (negatively charged) or N_s^+. As NV are obtained following charge transfer from N_s^0, it is expected that $[N_s^+] = [\mathrm{NV}]$, thus the total concentration of charges ($[N_s^+]+[\mathrm{NV}]$) is $\rho_C = 2[\mathrm{NV}] = 38 \pm 2$ ppb. The corresponding broadening contribution, $\Delta\nu_{1/2,\ \mathrm{charges}}$, is found following numerical calculation of the electric field[24]. This approach, detailed in SI, section S11 yields $\Delta\nu_{1/2,\ \mathrm{charges}} = a_{\mathrm{charges}} \times \rho_C^{2/3}$, with $a_{\mathrm{charges}} = 19.0\ \mathrm{kHz{\cdot}ppm}^{-2/3}$, which leads to $\Delta\nu_{1/2,\ \mathrm{charges}} = 2.15 \pm 0.08$ kHz. All determined contributions to the inhomogeneous broadening are summarized in Table 1. The ^{13}C contribution is found (by removing the contribution from the other terms) as $\Delta\nu_{1/2,13\mathrm{C}} = 216 \pm 6$ kHz, which corresponds to $T^*_{2,13\mathrm{C}} = 1.48 \pm 0.04$ μs.

Now, we point out that the ^{13}C spins occupying a considerable number of proximate carbon sites do not contribute to T_2^* of the primary lines. Looking at the FFT spectrum of half-echo in a wider frequency range (Fig. 4), one can see six sets of ^{13}C satellite lines accompanying the primary lines. We attribute these satellites to the carbon groups labeled in ODMR studies of single centers A(6), B(3), C(3), D(6), E(6)/F(3), and G(6)/H(3)[36,37]. When the magnetic field is oriented along the defect C_{3v} symmetry axis (as in Fig. 4), each carbon site consists of either three- or six-equivalent carbon atoms as indicated by the numbers in parentheses. In addition, weaker ^{13}C hf splittings are resolved as small shoulders at both sides of each primary line, and the three nearest-neighbor (NN) carbons sites are responsible for outer satellites, which are too far detuned from the primary lines to appear in the range of the FFT, owing to $A_{\mathrm{hfs}} \sim 130$ MHz[38]. The validity of our attribution of satellites is demonstrated by a spectral fit, shown as well in Fig. 4 (details in SI, section S10), in which the weights are constrained considering the number of equivalent carbon positions in each group. We find that the total count of carbons sites giving resolved satellites, distinct from the primary lines, equals 60. This important number is a consequence of the spread of the electronic spin density around the NV center, that results in strong A_{hfs} for some carbon sites (see also SI, section S10.3). Considering the 1.07% ^{13}C abundance, the probability of having zero ^{13}C spin in any of these 60 locations is $(1\text{–}0.0107)^{60} = 0.52$, which corresponds to the weight of the primary lines.

Having reviewed the contributions from all sources in Eq. (2) in the observed broadening of the primary lines in Fig. 2b, we have established that, for sample-A, the term related to magnetic dipolar interaction to distant ^{13}C is largely dominant. Removing the contribution from strain and local charges as well as that from other sources in Eq. (2) (see Table 1) we obtain, as the ^{13}C-imposed limit $T^*_{2,13\mathrm{C}} = 1.48 \pm 0.04$ μs. The ^{13}C occupying carbon sites among 60 lattice positions near the NV center do not contribute to the T_2^* of the primary lines but provide satellites.

Strain-induced splitting of optical transitions of individual single centers

The contribution of the zero-phonon line at 637 nm (1.945 eV) in the spin-conserving optical transitions between the $^3A_2$ ground state and the ^3E excited state is ~4% when compared to the whole fluorescence spectrum. At

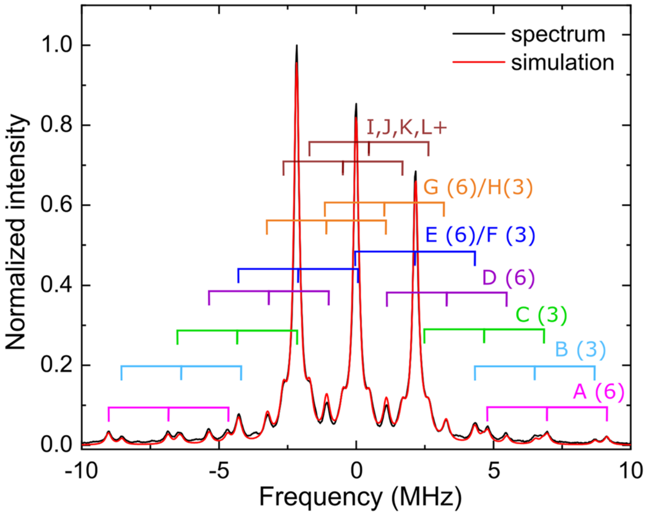

Fig. 4 | Wide-range view of the FFT spectrum of ensemble NV in sample-A. The spectrum for **B**//[111] (same acquisition data as in Fig. 2b) is fitted with a model including both primary lines and ^{13}C satellites. To describe the individual lines, we fixed $\Delta\nu_{1/2} = 248.7$ kHz as the Lorentzian broadening ($T_2^* = 1.28$ μs) consistently with the determination in Fig. 2b. We find the hyperfine splittings of groups A(6), B(3), C(3), D(6), E(6)/F(3), G(6)/H(3) to be $|A_{\mathrm{hfs}}| = 13.82, 12.90, 8.90, 6.50, 4.25$, and 2.17 MHz respectively. For the shoulders of the primary lines, corresponding to several unresolved carbon sites (that we label 'IJKL$^+$'), we obtain $|A_{\mathrm{hfs}}| = 0.96$ MHz. Detailed fit results are given in SI, Section S10.2.

room temperature, the ^{3}E excited state has two sub-levels, $|m_s = 0\rangle$ and $|m_s = \pm 1\rangle$, similar to the ^{3}A$_2$ ground state, however with a smaller zero-field splitting of 1.4 GHz. Non-resonant excitation using phonon-assisted optical absorption allows for initialization and readout—e.g., by shining 532 nm laser light. The ZPL, which is broadened owing to coupling of electronic excitations to phonons under ambient conditions, is narrowed with the decrease of temperature. At low temperature (< 10 K), the ^{3}E excited state is split into distinct sub-levels, therefore, the ZPL consists of several resonance lines.

While the electron spin-spin interaction splits the ^{3}A$_2$ triplet ground state into $|m_s = 0\rangle$ and $|m_s = \pm 1\rangle$ sublevels separated by the zero-field splitting ($D = 2.87$ GHz), the axial parts of the spin-orbit and electron spin-spin interactions split the ^{3}E triplet excited state into four levels, A_2, A_1, $E_{x,y}$, and $E_{1,2}$ (see SI, section S12)[39]. Under no strain, $E_{x,y}$ and $E_{1,2}$ are both doubly degenerate, and the resonant optical transitions between the ^{3}A$_2$ ground state and the ^{3}E excited state are either linearly polarized (for $|m_s = 0\rangle \leftrightarrow |E_{x,y}\rangle$) or circularly polarized (for $|m_s = \pm 1\rangle \leftrightarrow |A_2\rangle$, $|m_s = \pm 1\rangle \leftrightarrow |A_1\rangle$ and $|m_s = \pm 1\rangle \leftrightarrow |E_{1,2}\rangle$).

Strain lowers the C_{3v} symmetry and induces splitting, shifting and mixing of the excited state levels. As a result, excitation spectra of single NV centers show typically six spin-selective resonant transitions (SI, section S12)[12,15]. While the longitudinal strain shifts all sub-levels together, conserving the fine structure of optical spectrum, the transverse strain splits the sub-levels. The splitting (by $2\delta_\perp$) between E_x and E_y indicates the strength of the transverse strain. The mixing of the excited levels changes the polarization properties of the resonant optical transitions. At low strain, the mixing is small and consequently the polarization properties of the resonant optical transitions are preserved. In these conditions, the spin-selective resonant excitation provides access to high-fidelity initialization and readout[16], spin-photon entanglement[12], and was used for generation of indistinguishable photons[17,18] or entanglement between remote NV centers[13].

Therefore, engineering of diamond lattice with low strain, minimizing the presence of structural defects such as dislocation and stacking faults, is required. We choose high-crystalline-quality, high-purity (samples-B and -C of $[\mathrm{N_s^0}]_{\mathrm{avg}} = 3 \sim 4$ ppb) HPHT crystals grown using, as seed crystal, a defect-free (001)-oriented diamond. In the resulting HPHT crystals, the (001) growth sector, which extends straight upward from the seed surface, contains very few dislocations and stacking faults in the upper part[8]. Besides, the low nitrogen concentration ensures good spectral stability of the transitions[40].

The fine structure of the ^{3}E state is revealed by PLE (photoluminescence excitation) spectrum in which the resonant excitations by scanning a 637 nm tunable diode laser are detected by PL (photoluminescence) into the phonon side band. To detect all transitions, the ground state spin transition $|m_s = 0\rangle \rightarrow |m_s = \pm 1\rangle$ is continuously driven by microwave with resonance frequency 2.87 GHz, enabling the electronic transition connected to $m_s = \pm 1$. The splitting ($2\delta_\perp$) of the sub-levels connecting to the $m_s = 0$ ground state into E_x and E_y is proportional to the transverse strain ($\delta_\perp$), where 1 MPa corresponds to 1 GHz splitting[41]. Therefore, by measuring the splitting of the E_x and E_y levels, we can determine the local lattice strain probed by the NV center. The sensitivity is limited by the linewidth of the optical transitions, that is less than 12 MHz.

In sample-B and -C, single NV centers were observed in the central (001) sector. In the {110} sector, NV centers were not formed, as little nitrogen is incorporated. In the {111} sector, the NV centers were not detected, as a result of the preferential boron incorporation. Overall, in these samples, the percentage of NV centers showing $\delta_\perp < 2$ GHz is more than 60%, as shown in Fig. 5. With this weak perturbation ($\delta_\perp \lesssim 2$ GHz), E_x and E_y retain a sufficient $m_s = 0$ character, and the resonant excitation of a cyclic transition $|0\rangle_{^3A_2} \rightarrow |E_x\rangle$ or $|0\rangle_{^3A_2} \rightarrow |E_y\rangle$ allows high-fidelity readout. This also enables the generation of spin-photon entanglement, as illustrated in Togan et al.[12]: experiments utilizing the $|A_2\rangle$ state (which decays with equal probabilities to $|-1\rangle_{^3A_2}$ through σ_+-polarized photons and to $|+1\rangle_{^3A_2}$ through σ_--polarized photons) were possible using a single NV center with small strain splitting ($\delta_\perp \approx 1.28$ GHz).

Discussion

In the present work, $T_2^* = 1.280 \pm 0.016$ μs has been attained for a natural abundance HPHT crystal (sample-A). This is achieved through material control steps, which enable reducing the contributions to T_2^* from the different sources (Table 1).

The ^{13}C-limit is determined as $T^*_{2,13\mathrm{C}} = 1.48 \pm 0.04$ μs ($\Delta\nu_{1/2,13\mathrm{C}} = 216 \pm 6$ kHz), which exceeds the previously reported $T_2^* = 1$ μs[11,26]. It is likely that the high magnetic fields (≥ 1731 G) we employed play a considerable role in the difference to the previous determination, obtained at 150 G[11,26]. Indeed, theoretical work[42] predicted that $T_2^*{}_{13\mathrm{C}}$ in natural abundance varies with the bias magnetic field, through a transition range (100 G < B < 1000 G), in between a low-field limit of 1.63 μs, and a high-field limit of 2.92 μs. The origin of this variation is the change in the quantization axis for a ^{13}C spin in between low field ($\nu_{13\mathrm{C}} \ll A_{zz}$) and high field ($\nu_{13\mathrm{C}} \gg (A_{zx}{}^2 + A_{zy}{}^2 + A_{zz}{}^2)^{1/2} = A$) regimes[42]. Here, $\nu_{13\mathrm{C}}$ is the ^{13}C NMR frequency and $A_{zx,zy,zz}$ are elements of the hyperfine coupling tensor. This effect consistently explains variations of T_2^* reported in experiments on single NV[43].

In our results, ^{13}C at ~60 carbon sites (NN(nearest-neighbors)(3), A(6), B(3), C(3), D(6), E(6)/F(3), G(6)/H(3), IJKL$^+$(21), in decreasing order of the magnitude of hf splitting), provide separated ^{13}C satellites. The $T^*_{2,13\mathrm{C}}$ (primary lines) is determined by couplings to the ^{13}C sites giving weaker hf splitting, such as those labeled M, N, O in ref. 36, and further ones. At 1731 G ($\nu_{13\mathrm{C}} = 1.854$ MHz), ^{13}C sites contributing to $T_2^*{}_{13\mathrm{C}}$ satisfy $\nu_{13\mathrm{C}} \gg A$ so that our measurements (≥ 1731 G) belong to the high-field limit. In contrast, at $B = 150$ G ($\nu_{13\mathrm{C}} = 0.161$ MHz, as in ref. 11,26), an important number of ^{13}C sites contributing to the primary lines satisfy $\nu_{13\mathrm{C}} \ll A_{zz}$, indicating a regime closer to the low-field limit. Noticeably, our determination of $T^*_{2,13\mathrm{C}}$ lies lower than the theoretical estimate of $T^*_{2,13\mathrm{C}} = 2.92$ μs[42]. It is expected that our work should stimulate further theoretical studies considering factors determining $T^*_{2,13\mathrm{C}}$ revealed by our observation of the ^{13}C satellite lines: not only a number of carbon sites do not contribute to $T^*_{2,13\mathrm{C}}$, but also, significant delocalization of the NV center electronic wavefunction occurs[44].

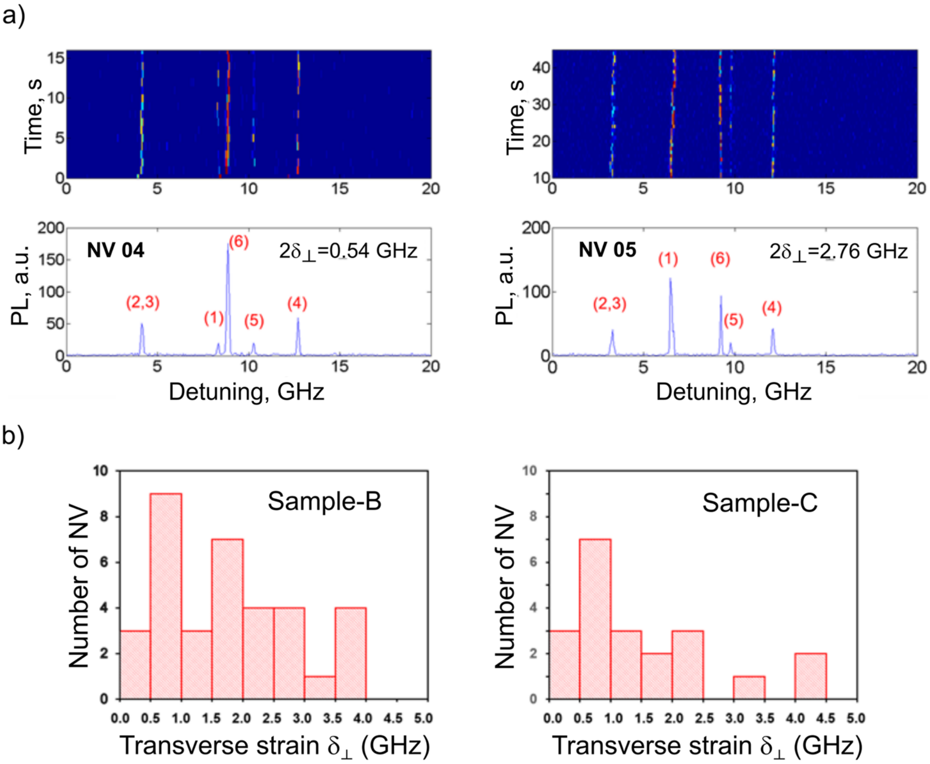

Fig. 5 | Summary of PLE experiments done in sample-B and -C at $T = 8$ K. **a** PLE spectra of two single NV (NV04 and NV05) in sample-B. The resonant optical excitations to the ^{3}E excited state sublevels, $|m_s = 0\rangle \rightarrow |E_y\rangle$, $|m_s = \pm1\rangle \rightarrow |E_2\rangle$, $|m_s = \pm1\rangle \rightarrow |E_1\rangle$, $|m_s = \pm1\rangle \rightarrow |A_2\rangle$, $|m_s = \pm1\rangle \rightarrow |A_1\rangle$ and $|m_s = 0\rangle \rightarrow |E_x\rangle$ are labeled from (1) to (6), respectively (see Supplementary Fig. 23). **b** Histograms showing the distribution of transverse strain ($\delta_\perp$) of single NV centers in sample-B and -C.

Our ^{13}C limit at natural abundance (1.07%) yields the proportionality constant in Eq. (3), $A_{^{13}\mathrm{C}} = 0.063 \pm 0.002\ \mathrm{ms}^{-1}\mathrm{ppm}^{-1}$. By 99.97% ^{12}C enrichment ([^{13}C] =0.03%), we predict the ^{13}C contribution to be reduced to $T^*_{2,13\mathrm{C}} \approx 50$ µs ($\Delta\nu_{1/2,13\mathrm{C}} = 6.0$ kHz). Keeping other contributions as in sample-A, $T_2^* > 10$ µs is predicted, for NV ensemble within the same large volume, without using sophisticated protocols such as spin-bath driving and DQ.

In sample-A, the terms from strain and local charges are smaller by one and two orders of magnitude, respectively, compared to that from the interaction with ^{13}C (Table 1). In sample-A, we have found $\Delta\nu_{1/2,\mathrm{strain+charges}} = 17 \pm 6$ kHz for NV within a >10mm^3 volume, which is compared to $\Delta\nu_{1/2,\mathrm{strain+charges}} = \Delta\nu_{1/2,\mathrm{allowed}} - 0.5 \times \Delta\nu_{1/2,\mathrm{DQ}} = 25.3$ kHz measured for 3×3×0.07 mm^3 in a CVD sample[45].

Looking at optical transitions, we noticed that a large fraction of single NV centers created in high-crystalline-quality and high-purity ([N$_s^0$]~3-4 ppb) HPHT crystals (sample-B and C) exhibit small transverse strain ($\delta_\perp < 2$ GHz) in spin-selective optical transitions between the sublevels of the ^{3}A$_2$ ground state and those of the ^{3}E excited state at low temperature (8 K).

Overall, our observations highlight that crystalline quality is of crucial importance, to preserve spin/optical transition properties. The density of dislocations is expected to be reduced both, in HPHT growth using high crystalline quality seed crystals[9], and in CVD growth using a low-strain HPHT substrate with proper surface processing (polishing and etching)[46], to similarly low levels. For further improvement, the growth in the diamond thermodynamic stability region (as in HPHT) might be favorable compared to CVD growth performed under non-equilibrium conditions. It was demonstrated that close-to-theoretical FWHM of the synchrotron X-ray rocking curve is achievable with the HPHT method[9,47]. The present work suggests HPHT growth is worth exploiting to attain superior crystal quality for quantum applications.

Methods

Samples

Three natural abundance (^{13}C: 1.07%) diamond crystals (samples-A~C) were grown by the temperature gradient method at high-pressure, high-temperature (HPHT) conditions of 5.5 GPa and 1350 °C using high-purity Fe-Co solvents to which nitrogen getter (Ti) was added. (001)-oriented seed crystals (0.5 mm × 0.5 mm plates) cut from high-crystalline quality type-IIa synthetic HPHT diamond crystals were used. Sample-A was irradiated with 2 MeV electrons (total fluence 6×10^{16} e/cm^2) at 800 °C and annealed at 1000 °C (2 h, in vacuum). See SI, section S2 for a description of the high-temperature irradiation setup used for sample-A. Samples-B and -C were irradiated with 2 MeV electrons at room temperature to the total fluence of 5×10^{10} e/cm^2 and 1×10^{11} e/cm^2, respectively followed by annealing at 1000 °C (2 h, in vacuum). See SI, section S1 for further information on the samples, including photographs.

X-ray topography

Synchrotron X-ray topography of sample-A was measured at the 1-km beamline (BL29XUL EH4) of Spring-8. The topographs with three different reflection indices were acquired under quasi-plane wave incidence using appropriate Si collimators (see SI, section S4, Supplementary Table 1 for details). The reflection beam images were taken by a CCD-based X-ray camera with a pixel size of 6.5 µm.

Electron paramagnetic resonance

Continuous-wave (cw)-EPR spectra were performed with a Bruker E500 X-band spectrometer. The slow-passage cw-EPR spectra of sample-A (Fig. 1d) were taken using the 100 kHz magnetic field modulation with the amplitude 1 µT, field scan rate 1 mT/168 s, microwave power 0.2 µW. The signals are partly saturated by the microwave power and broadened by the 100 kHz (0.0035 mT) modulation. For measuring low concentrations of N$_s^0$ which is easily saturated by the microwave power, standard slow-passage conditions are not favorable for attaining signal sensitivity. For quantifying [N$_s^0$] of sample-B and -C, rapid-passage technique[19,48] was employed by using a Bruker ER4122SHQ cavity (the loaded Q-factor: $Q_L \sim 10{,}000$). Details on the rapid-passage EPR acquisitions for sample-B and -C and corresponding EPR spectra are available in SI, section S3. [N$_s^0$]$_{\mathrm{avg}}$ measured for samples B and -C are 4 ppb and 3 ppb, respectively. Suffix "avg" indicates that these (100)-oriented HPHT plates have non-uniform distributions of N$_s^0$.

Spatial distribution of N_s^0 of unirradiated sample-A was characterized by EPR imaging using high-power gradient accessory Bruker E540 GCX2 (2D gradients with 20 mT/cm) and Bruker ER4108 TMHS resonator. Rapid-passage technique was utilized in the imaging measurement[48].

Pulsed EPR measurements were carried out using a Bruker ELEXSYS E580 X-band spectrometer, together with a 9.5" magnet. Elements of the EPR bridge used in pulse acquisitions are represented in SI, section S6.2. The concentration of N_s^0 in sample-A was measured by utilizing instantaneous diffusion effect in two-pulse echo decay. While the EPR linewidth is affected by dipolar broadening among all paramagnetic species present, the instantaneous spectral diffusion effect is determined by the dipolar interaction only among the fraction of electron spins that are excited by the microwave (MW) pulses. Pulse sequence ($\theta_p/2$ — τ — θ_p — τ — echo) was used for measurement before electron irradiation. The flip angle θ_p was varied by varying the pulse height fixing the pulse durations of the first and the second pulses at 16 ns and 32 ns, respectively. Pulse sequence ($\pi/2$ — τ — θ_p — τ — echo) was used for the measurement of $[N_s^0]$ after electron irradiation and subsequent annealing. The flip angle θ_p was adjusted by the duration of the pulse t_p, after measuring that 32 ns corresponds to an inversion ($t_p = 32\ \text{ns} \cdot \theta_p/\pi$).

For NV FID or echo acquisitions, the Bruker SpinJet AWG was used and acquisitions were made in transient recorder mode. Experiments were performed under CW illumination with green (532 nm) light, 200 mW, to enhance the EPR signal. The initial part (~ 100 ns) of the FID is not detected, which corresponds to the so-called deadtime, typical of pulsed EPR experiments. The deadtime is an interval during which the signal is prevented from reaching the preamplifier, to protect the components in the detection channel from high power microwave. The latter can occur both due to the ringing following pulses, and to the noise of the traveling wave tube amplifier (TWTA). For the allowed transition of NV (data in Fig. 2) the π pulse duration was 20 ns and the pulse spacing τ was chosen, so as to minimize Electron Spin Echo Envelope Modulation (ESEEM) effects on the ^{13}C satellites, which can be made by choosing τ near a revival in a standard ESEEM measurement ($\pi/2$ — τ — π — τ — echo). Optimal value was found at τ = 330 ns for the allowed transition at $B = 2436$ G. 4-steps phase cycling was used to compensate for the effect of pulse and detection errors. To avoid artefacts related to leakage microwave within the EPR bridge, the pulses were defined using the Bruker SpinJet AWG so that the excitation carrier frequency (ν_{MW}) is offset from that of the microwave Gunn source (ν_{Gunn}) of the bridge. For the allowed transitions, the offset was set to 5.6 MHz. The pulse carrier frequency was made resonant with the central ($m_I = 0$) line of the NV hyperfine structure (thus, due to the applied offset, the frequency of the Gunn source was detuned by 5.6 MHz from the central line). Effects of amplification of leakage signals, that occur typically at the microwave frequency of the Gunn diode, are therefore efficiently avoided, which allows obtaining a distortion-free signal. The detection was made in quadrature mode. Thus, while, in the figures, only the real part of the time domain signal is represented, it consists, in fact, of two quadrature components (real and imaginary). In the EPR bridge, the signal is demodulated at the frequency ν_{Gunn}. The as-recorded signal was numerically transformed ($\times\, e^{2i\pi(\nu_{\text{Gunn}}-\nu_{\text{MW}})t}$), to re-center the spectrum with respect to the excitation frequency ν_{MW} as detailed in SI, section S6.2. Both quadratures of the time-domain signal were used to compute the FFT (in the figures, only the real part of the FFT is shown).

For acquisition of the NV forbidden $\Delta S_Z \approx 2$ transition signal (Fig. 3), a similar protocol was employed as for the allowed transitions (in particular, the same illumination conditions were applied). However, a few modifications were made to adapt to the significantly lower dipole. First, in order to perform efficient driving and improve S/N, the resonator Q-factor was increased to $Q \sim 300$. Second, the FFT shown in Fig. 3b was performed on full echoes, instead of half-echoes, providing another slight increase in S/N. As in the allowed transition measurement, the microwave excitation frequency was detuned from the Gunn diode frequency, here using 11 MHz detuning (to avoid driving any of the ^{14}N $m_I = -1, 0, +1$ satellites). The Gunn diode frequency was set to 9.691 GHz, so that the 11 MHz-detuned excitation matches the precise resonator dip position, found at $\nu_{\text{Res}} = 9.68$ GHz. The interpulse spacing τ = 8200 ns was used in the Hahn-echo (in order to be able to record the time trace over a sufficient duration before the echo maximum). At a certain microwave power, the Rabi frequency for the half-field transition depends on the magnetic field tilt angle Θ. Here, the microwave power was adjusted, for each echo in Fig. 3b to ensure constant Rabi $\Omega_1 = (2\pi)\ 3.125$ MHz, corresponding to a 160ns-long π pulse. Further details on the acquisition protocol for the forbidden $\Delta S_Z \approx 2$ transition including precise measurement parameters (such as microwave power, number of averages) are given in SI, section S9.

To determine the magnetic field inhomogeneity in the NV ensemble volume of sample-A, we observe the T_2^* for the $m_s = 0 \leftrightarrow -1$ transition of NV, by setting the magnetic field to $B = 4480$ G and repeating the acquisition and analysis as in Fig. 2. The corresponding echo and FFT shown in Supplementary Fig. 14 provide $T_2^* = 1.228 \pm 0.012$ μs, corresponding to $\Delta\nu_{1/2}^{4480\text{G}} = 259.2 \pm 2.5$ kHz. The widths $\Delta\nu_{1/2}$ of the primary lines obtained in the different measurements described in our manuscript, at fields 1731 G (DQ in Fig. 3), 2436 G (allowed $m_s = 0 \leftrightarrow +1$ transition, Fig. 2) and 4480 G (allowed, $m_s = 0 \leftrightarrow -1$ transition, Supplementary Fig. 14) obey:

$$0.5 \times \Delta\nu_{1/2,\text{DQ}}^{1731\text{G}} = \Delta\nu_{1/2,\text{NV}-[13\text{C},\text{N}_s^0,\text{NV}]} + \Delta\nu_{1/2,B-\text{inhom}}^{1731\text{G}} + \Delta\nu_{1/2,1/T_2},$$

$$\begin{aligned}\Delta\nu_{1/2}^{2436\text{G}} =& \Delta\nu_{1/2,\text{NV}-[13\text{C},\text{N}_s^0,\text{NV}]} + \Delta\nu_{1/2,B-\text{inhom}}^{2436\text{G}} + \Delta\nu_{1/2,1/T_2} \\ &+ \Delta\nu_{1/2,\text{strain+charges}},\end{aligned}$$

$$\begin{aligned}\Delta\nu_{1/2}^{4480\text{G}} =& \Delta\nu_{1/2,\text{NV}-[13\text{C},\text{N}_s^0,\text{NV}]} + \Delta\nu_{1/2,B-\text{inhom}}^{4480\text{G}} + \Delta\nu_{1/2,1/T_2} \\ &+ \Delta\nu_{1/2,\text{strain+charges}},\end{aligned}$$

where $\Delta\nu_{1/2,\text{NV}-[13\text{C},\text{N}_s^0,\text{NV}]}$ represents the total contribution from NV-^{13}C, NV-N_s^0, NV-NV interaction. In between the 2436 G and 4480 G measurements, only the contribution from the bias field inhomogeneity is expected to change. The magnetic field inhomogeneity (ΔB) is expected to increase linearly with the set magnetic field[49]. It follows:

$$\begin{aligned}\frac{\Delta B}{B} &= \frac{\Delta\nu_{1/2}^{4480\,\text{G}} - \Delta\nu_{1/2}^{2436\,\text{G}}}{(g_{||}\mu_B) \times (4480\,\text{G} - 2436\,\text{G})} \\ &= \frac{(259.2\,\text{kHz} - 248.7\,\text{kHz})}{(2.8032\,\text{MHz}\,\text{G}^{-1}) \times (4480\,\text{G} - 2436\,\text{G})} = 1.83 \pm 0.73\,\text{ppm}\end{aligned}$$

Correspondingly, the contribution of the bias field inhomogeneity to the quantities $\Delta\nu_{1/2}^{2436\text{G}}$ and $0.5 \times \Delta\nu_{1/2,\text{DQ}}^{1731\text{G}}$ is found to be $\Delta\nu_{1/2,B-\text{inhom}}^{2436\text{G}} = 12.5 \pm 4.9\text{kHz}$ and $\Delta\nu_{1/2,B-\text{inhom}}^{1731\text{G}} = 8.9 \pm 3.5\text{kHz}$, respectively. The difference in the bias field inhomogeneity must be taken into account when extracting the contribution from strain and local charges from the values of $\Delta\nu_{1/2,\text{allowed}}$ (determined at 2436 G) and $0.5\times\Delta\nu_{1/2,\text{DQ}}$ (determined at 1731 G): $\Delta\nu_{1/2,\text{allowed}} - 0.5 \times \Delta\nu_{1/2,\text{DQ}} = \Delta\nu_{1/2,\text{strain+charges}} + \delta_{\text{inhom}}$ where the contribution from the difference in bias field inhomogeneity is $\delta_{\text{inhom}} = \Delta\nu_{1/2,B-\text{inhom}}^{2436\text{G}} - \Delta\nu_{1/2,B-\text{inhom}}^{1731\text{G}} = 3.6 \pm 1.4\text{kHz}$.

PLE measurements

Low temperature PLE (photoluminescence excitation) experiments were performed using home-built confocal microscope setup to address individual NV centers optically. The setup is described in Supplementary Fig. 24. The sample is inside a Janis ST-500 cold finger Helium flow cryostat at $T = 8$ K. The off-resonant 532 nm laser (CNI Laser) polarizes the $^3A_2$ ground state into $m_s = 0$. The resonant excitation to the ^3E excited state sublevels is carried out with tunable narrow-band 637 nm laser (Velocity New Focus). Both lasers are pulsed by a double-pass AOM configuration to get over 60 dB on/off ratio. The PL (photoluminescence) is collected by a Nikon LU Plan Fluor 100× air objective (N.A. = 0.9) mounted on a NPoint NPXY100Z25 − 102 nanoposition stage. With scanning the frequency of the tunable narrow-band laser, the phonon side band emission is detected by Perkin-Elmer avalanche photodiodes (APDs) after Semrock FF01-731/137-25 filter. In order to observe all six optical transitions from the ground state sublevels, microwave excitation is applied. When microwave is not applied, only $|m_s = 0\rangle \rightarrow |E_y\rangle$ and $|m_s = 0\rangle \rightarrow |E_x\rangle$ transitions are observed. The microwave source is a Rohde&Schwarz SMIQ signal generator. Triple switches (from Minicircuits) in serial configuration yields over 180 dB on/off ratio to minimize the leakage. Rubidium atomic clocks are used to synchronize timing among the equipment and to stabilize frequencies of the MW/RF outputs. The FPGA based 12-channel pulse generator with 1.5 ns resolution controls the pulsing sequence. The other FPGA board is designed as the time resolved counting system with 20 ps resolution. Both are from Swabian Instruments.

Data availability

All data supporting the findings in this study is available from the corresponding author upon (reasonable) request.

Received: 18 February 2024; Accepted: 25 September 2024;

References

1. Achard, J., Jacques, V. & Tallaire, A. Chemical vapour deposition diamond single crystals with nitrogen-vacancy centres: a review of material synthesis and technology for quantum sensing applications. *J. Phys. D: Appl. Phys.* **53**, 313001 (2020).
2. Markham, M. L. et al. CVD diamond for spintronics. *Diam. Relat. Mater.* **20**, 134–139 (2011).
3. Teraji, T. et al. Homoepitaxial diamond film growth: High purity, high crystalline quality, isotopic enrichment, and single color center formation: Homoepitaxial diamond film growth. *Phys. Status Solidi (a)* **212**, 2365–2384 (2015).
4. Michl, J. et al. Perfect alignment and preferential orientation of nitrogen-vacancy centers during chemical vapor deposition diamond growth on (111) surfaces. *Appl. Phys. Lett.* **104**, 102407 (2014).
5. Ohno, K. et al. Engineering shallow spins in diamond with nitrogen delta-doping. *Appl. Phys. Lett.* **101**, 082413 (2012).
6. Watanabe, H., Nebel, C. E. & Shikata, S. Isotopic homojunction band engineering from diamond. *Science* **324**, 1425–1428 (2009).
7. Strong, H. M. & Wentorf, R. H. The growth of large diamond crystals. *Naturwissenschaften* **59**, 1–7 (1972).
8. Sumiya, H. & Satoh, S. High-pressure synthesis of high-purity diamond crystal. *Diam. Relat. Mater.* **5**, 1359–1365 (1996).
9. Sumiya, H., Harano, K. & Tamasaku, K. HPHT synthesis and crystalline quality of large high-quality (001) and (111) diamond crystals. *Diam. Relat. Mater.* **58**, 221–225 (2015).
10. Burns, R. C. et al. HPHT growth and x-ray characterization of high-quality type IIa diamond. *J. Phys.: Condens. Matter* **21**, 364224 (2009).
11. Barry, J. F. et al. Sensitivity optimization for NV-diamond magnetometry. *Rev. Mod. Phys.* **92**, 015004 (2020).
12. Togan, E. et al. Quantum entanglement between an optical photon and a solid-state spin qubit. *Nature* **466**, 730–734 (2010).
13. Bernien, H. et al. Heralded entanglement between solid-state qubits separated by three metres. *Nature* **497**, 86–90 (2013).
14. Pfaff, W. et al. Unconditional quantum teleportation between distant solid-state quantum bits. *Science* **345**, 532–535 (2014).
15. Batalov, A. et al. Low temperature studies of the excited-state structure of negatively charged nitrogen-vacancy color centers in diamond. *Phys. Rev. Lett.* **102**, 195506 (2009).
16. Robledo, L. et al. High-fidelity projective read-out of a solid-state spin quantum register. *Nature* **477**, 574–578 (2011).
17. Bernien, H. et al. Two-photon quantum interference from separate nitrogen vacancy centers in diamond. *Phys. Rev. Lett.* **108**, 043604 (2012).
18. Sipahigil, A. et al. Quantum interference of single photons from remote nitrogen-vacancy centers in diamond. *Phys. Rev. Lett.* **108**, 143601 (2012).
19. Felton, S. et al. Hyperfine interaction in the ground state of the negatively charged nitrogen vacancy center in diamond. *Phys. Rev. B* **79**, 075203 (2009).
20. Vanoort, E. & Glasbeek, M. Electric-field-induced modulation of spin echoes of N-V centers in diamond. *Chem. Phys. Lett.* **168**, 529–532 (1990).
21. Dolde, F. et al. Electric-field sensing using single diamond spins. *Nat. Phys.* **7**, 459–463 (2011).
22. Doherty, M. W. et al. Theory of the ground-state spin of the NV center in diamond. *Phys. Rev. B* **85**, 205203 (2012).
23. Udvarhelyi, P., Shkolnikov, V. O., Gali, A., Burkard, G. & Pályi, A. Spin-strain interaction in nitrogen-vacancy centers in diamond. *Phys. Rev. B* **98**, 075201 (2018).
24. Mittiga, T. et al. Imaging the local charge environment of nitrogen-vacancy centers in diamond. *Phys. Rev. Lett.* **121**, 246402 (2018).
25. Kittel, C. & Abrahams, E. Dipolar broadening of magnetic resonance lines in magnetically diluted crystals. *Phys. Rev.* **90**, 238–239 (1953).
26. Bauch, E. et al. Ultralong dephasing times in solid-state spin ensembles via quantum control. *Phys. Rev. X* **8**, 031025 (2018).
27. Yamamoto, T. et al. Extending spin coherence times of diamond qubits by high-temperature annealing. *Phys. Rev. B* **88**, 075206 (2013).
28. Zhang, S., Ke, S. C., Zvanut, M. E., Tohver, H. T. & Vohra, Y. K. *g* tensor for substitutional nitrogen in diamond. *Phys. Rev. B* **49**, 15392–15395 (1994).
29. Zhang, S., Ke, S. C., Zvanut, M. E., Tohver, H. T. & Vohra, Y. K. Erratum: *g* tensor for substitutional nitrogen in diamond. *Phys. Rev. B* **51**, 8688–8688 (1995).
30. Wellbourn, C. M., Cooper, M. & Spear, P. M. De Beers natural versus synthetic diamond verification instrument. *Gem & Gemology*, 156–169 (1996).
31. Isoya, J. et al. ESE and cw-ESR studies of synthetic diamond crystals: distribution of nitrogen and nickel. In *1st International Conference of New Diamond Science and Technology*, (eds. S. S., F. O., Y. M.) 357–361 (KTK Science Publishing, Tokyo, Japan, 1988).
32. Salikhov, K. M., Dzuba, S. A. & Raitsimring, A. M. The theory of electron spin-echo signal decay resulting from dipole-dipole interactions between paramagnetic centers in solids. *J. Magn. Reson. (1969)* **42**, 255–276 (1981).
33. Ferrari, A. M., D'Amore, M., El-Kelany, K. E., Gentile, F. S. & Dovesi, R. The NV^0 defects in diamond: a quantum mechanical characterization through its vibrational and electron paramagnetic resonance spectroscopies. *J. Phys. Chem. Solids* **160**, 110304 (2022).
34. Fischer, R., Jarmola, A., Kehayias, P. & Budker, D. Optical polarization of nuclear ensembles in diamond. *Phys. Rev. B* **87**, 125207 (2013).
35. Segawa, T. F. & Shames, A. I. How to identify, attribute, and quantify triplet defects in ensembles of small nanoparticles. *J. Phys. Chem. Lett.* **11**, 7438–7442 (2020).
36. Dreau, A., Maze, J. R., Lesik, M., Roch, J. F. & Jacques, V. High-resolution spectroscopy of single NV defects coupled with nearby C-13 nuclear spins in diamond. *Phys. Rev. B* **85**, 134107 (2012).
37. Smeltzer, B., Childress, L. & Gali, A. C-13 hyperfine interactions in the nitrogen-vacancy centre in diamond. *N. J. Phys.* **13**, 025021 (2011).
38. Loubser, J. H. N. & van Wyk, J. A. Optical spin-polarisation in a triplet state in irradiated and annealed type Ib diamonds. In *Diamond Research* (ed. Daniel, P.) 11–14 (De Beers Industrial Diamond Division, Ascot, 1977).
39. Doherty, M. W. et al. The nitrogen-vacancy colour centre in diamond. *Phys. Rep.* **528**, 1–45 (2013).
40. Tamarat, P. et al. Stark shift control of single optical centers in diamond. *Phys. Rev. Lett.* **97**, 083002 (2006).

41. Davies, G. & Hamer, M. F. Optical studies of the 1.945 eV vibronic band in diamond. *Proc. R. Soc. Lond. A. Math. Phys. Sci.* **348**, 285–298 (1976).
42. Hall, L. T., Cole, J. H. & Hollenberg, L. C. L. Analytic solutions to the central-spin problem for nitrogen-vacancy centers in diamond. *Phys. Rev. B* **90**, 075201 (2014).
43. Maze, J. R. et al. Free induction decay of single spins in diamond. *New J. Phys.* **14**, 103041 (2012).
44. Gali, A., Fyta, M. & Kaxiras, E. Ab initio supercell calculations on nitrogen-vacancy center in diamond: Electronic structure and hyperfine tensors. *Phys. Rev. B* **78**, 155206 (2008).
45. Barry, J. F. et al. Sensitive AC and DC magnetometry with nitrogen-vacancy center ensembles in diamond. *arXiv:2305.06269* (2023).
46. Friel, I. et al. Control of surface and bulk crystalline quality in single crystal diamond grown by chemical vapour deposition. *Diam. Relat. Mater.* **18**, 808–815 (2009).
47. Shevyrtalov, S. et al. Towards high-quality nitrogen-doped diamond single crystals for X-ray optics. *J. Synchrotron Radiat.* **28**, 104–110 (2021).
48. Umeda, T. et al. Negatively charged boron vacancy center in diamond. *Phys. Rev. B* **105**, 165201 (2022).
49. Poole, C. P. *Electron Spin Resonance*, *Second Edition*, *A Comprehensive Treatise on Experimental Techniques*. (Wiley, New York, 1983), pp. 212-218.

Acknowledgements

This work was carried out under the collaboration agreement among University of Tsukuba, Ulm University and University of Stuttgart. The X-ray topography experiments were performed with the approval of RIKEN (Proposal No. 20220018). S.O and J.I acknowledge support by SCICORP (JST) and the Japan Society of the Promotion of Science (JSPS) KAKENHI (26246001). F.J. acknowledges support by EU via projects FLORIN, QuMicro and ERC grant HyperQ (no. 856432), QUANTERA via the project “Microfluidics Quantum Diamond Sensor”, Carl Zeiss Foundation via IQST, QPHOTON and Ultrasens-Vir projects, DFG via EXC 2154 (POLiS - Post Lithium Storage Cluster of Excellence), SFB 1279 (Exploiting the Human Peptidome for Novel Antimicrobial and Anticancer Agents), projects 491245864, 499424854 and 387073854. J.W. acknowledges support by the Max Planck Society, the EU via project AMADEUS (project 101080136), the BMBF via project DiaQnos (project 13N16455) and QSENS (projects 03ZU1110DC and 03ZU1110FE**)**.

Author contributions

R.B., Y.M. and J.I performed and analyzed pulsed EPR measurements. T.H.T., A.M., S.Y. and P.S. carried out PLE measurements. H.S. grew diamond crystals. K.T. and T.O. performed XRT experiments. N.M. and H.T. developed high temperature electron irradiation. S.O. performed electron irradiation. H.H. conducted EPR imaging experiments. F.J., J.W. and J.I. conceived the study. R.B., T.H.T. and J.I. wrote the manuscript with the inputs from all others. All authors discussed the results and commented on the manuscript.

Funding

Open Access funding enabled and organized by Projekt DEAL.

Competing interests

The authors declare no competing interests.

Additional information

Supplementary information The online version contains supplementary material available at https://doi.org/10.1038/s43246-024-00660-8.

Correspondence and requests for materials should be addressed to Rémi Blinder.

Peer review information *Communications Materials* thanks Dmitry Budker and the other, anonymous, reviewer(s) for their contribution to the peer review of this work. Primary Handling Editors: Rostislav Hrubiak and Aldo Isidori. A peer review file is available.